Asian Journal of Chemistry; Vol. 33, No. 2 (2021), 411-422

ASIAN JOURNAL OF CHEMISTRY

https://doi.org/10.14233/ajchem.2021.22979

Synthesis, Characterization, Photocatalytic and Electrochemical Studies of Reduced Graphene Oxide Doped Nickel Oxide Nanocomposites

VENKATACHALAM MANIKANDAN, RAMAKRISHNAN ELANCHERAN, PALANISAMY REVATHI, UMAPATHY VANITHA, PALANI SUGANYA and KUPPUSAMY KRISHNASAMY*

Department of Chemistry, Annamalai University, Annamalai Nagar-608002, India

*Corresponding author: E-mail: krishnasamybala56@gmail.com

Received: 3 September 2020; *Accepted*: 10 December 2020; *Published online*: 15 January 2021; AJC-20230

Elimination of organic pollutants from waste waters under the sunlight irradiation is a venerable challenge in the fields of environmental and materials science. This work aims to the fabrication of novel self-assembled, controlled rGO@NiO nanocomposite using eco-friendly simple co-precipitation method. The crystallite size, morphology and optical properties of the rGO, NiO and rGO@NiO were characterized using TG/DTA, FTIR, UV, XRD, SEM with EDAX and TEM techniques. The optical bandgap of the pure NiO, rGO and rGO@NiO nanocomposites was estimated as 3.75, 5.43 and 3.64 eV, respectively. Hence rGO@NiO nanocomposite might be considered as a semiconductor and can be utilized as a photocatalyst. The photocatalytic activity of prepared rGO@NiO nanocomposite was evaluated by using rhodamine B and methyl violet dyes. The degradation results revealed that almost 90% of dye degradation is carried out within a period of 60 min. The cyclic voltammetry studies indicated that the prepared rGO@NiO nanomaterials exhibited appreciable super capacitance value (233 F g^{-1}) at a current density of 1 A g^{-1}.

Keywords: Photocatalytic, Supercapacitor, Reduced graphene oxide, Nickel oxide, Co-precipitation method.

INTRODUCTION

Water pollution can be caused by many sources but industrial pollution of water is a salient issue. In previous decades, the efficiency of photocatalytic activity to degrade the organic pollutants by semiconductor metal-oxide such as NiO nanoparticle has drawn much public attention. It is due to the fact that NiO has high transparency and is considered as a p-type semiconductor with a broad band gap value around 3.2-4.0 eV [1,2].

Graphene oxide can be practically referred to as a functionalized graphene with various oxygen-bearing groups (*e.g.*, C=O, C–O and –OH), while r-GO is normally obtained through chemical reduction of GO [3,4]. The literature survey revealed that rGO/NiO [5-7], r-GO/TiO_2 [8-10], r-GO/SnO_2 [11-13], GO/ZnO [14-16] and rGO/$Ni(OH)_2$ [17-19], were used as an effective photocatalyst, sensors and photovoltaic materials. The GO, NiO and rGO@NiO nanostructure are also used as a promising capacitor material [20]. The specific capacitance of nanocomposites were normally lesser than 600 F g^{-1} whereas the recently reported rGO@NiO sheet-on-sheet composite shows a stable charge capacity of 1,031 mAh g^{-1} (at 0.1 ºC) after 40 charge-discharge cycles in Li-battery applications [21,22]. Considering the literature importance of nanomaterials, this research article focuses on the synthesis of NiO and rGO@NiO nanomaterials *via* the co-precipitation method and its photocatalytic activity with crystal violet and rhodamine-B organic dyes has been studied. The XRD analysis of the synthesized samples was performed to know the phase purity and crystallite size of the synthesized nanomaterials. Scanning electron microscopy (SEM) and transmission electron microscopy (TEM) techniques were used to study the surface morphology and particle size of the prepared samples. The super capacitor performance of the synthesized nanomaterials was investigated using cyclic voltammetry and electrochemical impedance spectroscopy (EIS) and the observed analytical results were suitably discussed in this work.

EXPERIMENTAL

The required chemicals such as graphite flakes, nickel chloride hexahydrate ($NiCl_2 \cdot 6H_2O$), sodium hydroxide, sulfuric

acid (98%), potassium permanganate (99.9%), hydrogen peroxide (30%) and hydrochloric acid (37%) were procured from Sigma-Aldrich and used without further purifications.

Synthesis of reduced graphene oxide (rGO): To a solution of 46 mL sulfuric acid, 1 g of graphite flakes and 1 g of sodium nitrate were added under the ice-cold condition and stirred for 4 h. Further, 6 g of potassium permanganate, which is a strong oxidizing agent was added slowly to the suspension. Then the mixture was stirred continuously for 2 h at 35 °C until the colour changes to brownish. Finally, the above mixture was quenched with 3 mL of hydrogen peroxide followed by the treatment of 10% HCl and centrifuged until reaches to neutral pH. After centrifugation, a gel-like suspension was obtained and dried in vacuum hot air oven at 60 ºC for 12 h to obtain graphene oxide nanosheet [23]. The flow chart of the synthesis of rGO is presented in Fig. 1.

Synthesis of nickel oxide nanoparticles: In a typical procedure, 8 g of $NiCl_2·6H_2O$ was dissolved in 60 mL of deionized water and subsequently 6 g of NaOH was dissolved in 40 mL of deionized water. The above-prepared nickel chloride solution was stirred at room temperature for about 1 h to achieve a homogeneous solution. Sodium hydroxide solution was added further to the above solution followed by the formation of the light green colour precipitate. The resultant precipitate was washed with deionized water and ethanol several times to remove the byproducts and impurities and dried at 60 ºC for 4 h to form $Ni(OH)_2$. The synthesized $Ni(OH)_2$ was calcinated at 450 ºC for 2 h in muffle furnace to obtain NiO nanoparticles. The synthesized NiO nanoparticles were used for further characterization. The schematic representation of the synthesis of NiO nanoparticles is shown in Fig. 2.

Synthesis of graphene oxide/nickel oxide (rGO@NiO) nanocomposite: Graphene oxide (20 mg) was dispersed in 20 mL of deionized water using an ultrasonic bath for 30 min. Then 27 mg of $NiCl_2·6H_2O$ was dissolved in 2 mL of deionized water. Then the above two solutions were mixed and stirred for 2 h followed by the addition of NaOH solution. The precipitate so obtained was filtered to get the $rGO/Ni(OH)_2$. This

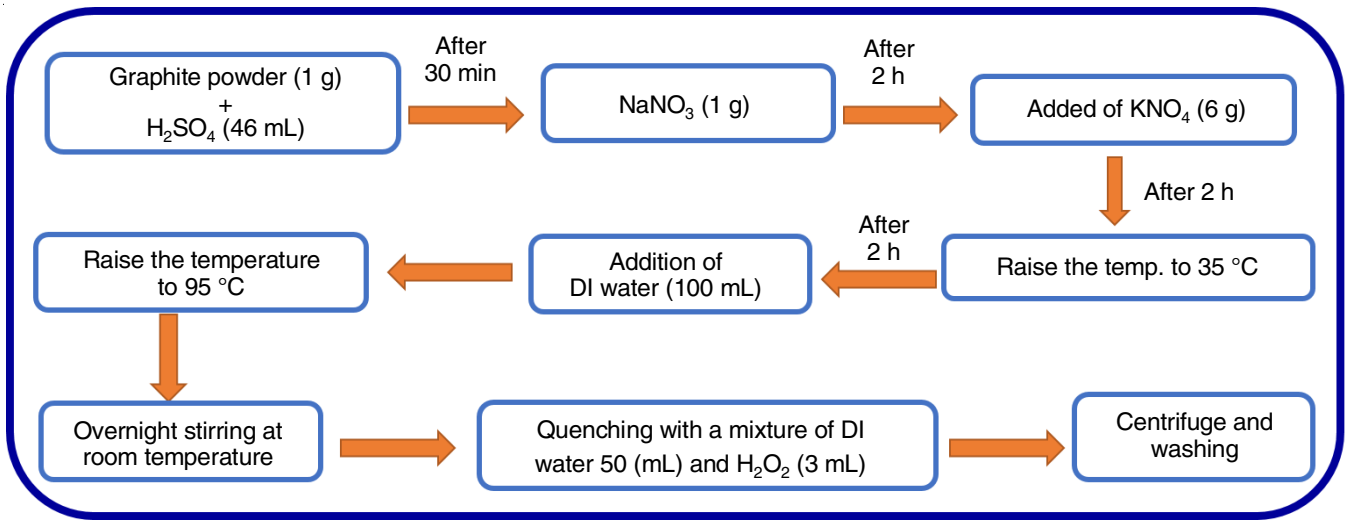

Fig. 1. Schematic diagram of the preparation of rGO using modified Hummer's method

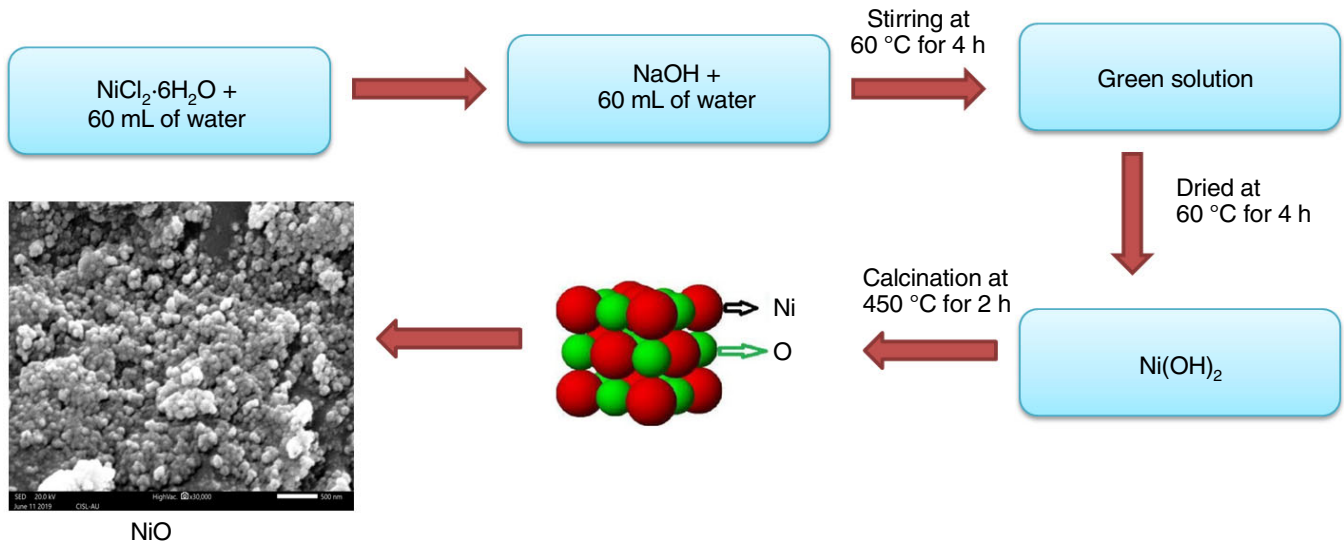

Fig. 2. Schematic diagram of the preparation of NiO nanoparticles

was followed by the calcination process for 2 h at 750 ºC to produce the rGO@NiO nanocomposite. The schematic representation of synthesis rGO@NiO nanocomposite shown in Fig. 3.

Characterization: The UV-vis absorption spectra were recorded on a Varian Cary 50 spectrometer using a quartz cell with 1 cm optical path. Fourier transform infrared (FTIR) spectra were recorded on a Bruker tensor 27 instrument, under the wavelength of 4000-400 cm^{-1} range and the sample was prepared by KBr pellet method. Thermogravimetric (TGA) measurements were carried out in the thermal analyzer (STA449 F3 Jupiter) under N_2 gas flow at a heating rate of 10 ºC per min. The X-ray diffraction patterns of the catalyst were measured with a Model D/max-RC X-ray diffractometer using CuKα radiation source (λ = 1.5418 Å) as the incident radiation. Transmission electron microscopy measurements were carried out on a Hitachi-7650 transmission electron microscope operated at an accelerated voltage of 80 kV. Energy-dispersive X-ray spectroscopy (EDX) and SEM measurements were carried out on JSM-5610LV. Electrochemical measurements were carried out in a CHI 660C (CH Instruments, Shanghai, China) electrochemical workstation with a conventional three-electrode system with a Pd-PG or Pd-CCG modified glassy carbon electrode as the working electrode, platinum wire and an Ag/AgCl (saturated KCl) as the counter and the reference electrode, respectively at room temperature.

Photocatalytic measurement: The photocatalytic activity of NiO and rGO@NiO was evaluated by the degradation of aqueous solutions of the methyl violet and rhodamine B using sun-light as a radiation source. For the degradation process, 10^{-4} M of dye solutions were fixed as an optimized concentration for both the dyes and mixed with 500 mL distilled water. A dye solution (50 mL) was taken in a 100 mL beaker and the catalyst (20 mg for methyl violet/30 mg for rhodamine B) was added into the solution. The solution was stirred with a magnetic stirrer for 90 min. The solution of both dyes were collected in every 10 min for the UV analysis to evaluate the degradation efficiency of the prepared nanocatalysts.

RESULTS AND DISCUSSION

Thermal gravimetric/differential thermal analysis of rGO@NiO nanocomposite: The typical thermal analysis curve of $Ni(OH)_2$ and rGO@$Ni(OH)_2$ are shown in Fig. 4a and 4b, respectively. Thermal behaviour of the synthesized $Ni(OH)_2$ nanoparticles was investigated by DTA analysis. The thermal weight loss of $Ni(OH)_2$ (Fig. 4a) has occurred in three steps. The first weight loss from room temperature to 135 ºC was due to the dehydration and evaporation of free water from the starting precursor, which resulted in a weight loss of about 13%. The second degradation of weight loss is observed at about 135 to 315 ºC that corresponds to 15%. This is due to the dihydroxylation of $Ni(OH)_2$, which leads to the transformation of NiO. Above 315 ºC, the product remains stable without mass loss, indicating the thermal stability of the crystalline NiO sample. Hence TGA analysis confirms the required temperature for the formation of NiO from the starting precursor. The exothermic peak at about 400 ºC exhibited obviously due to the decalescence phenomena, possibly resulting from amorphous to crystalline phase [24]. Fig. 4b is the TG-DTA curve

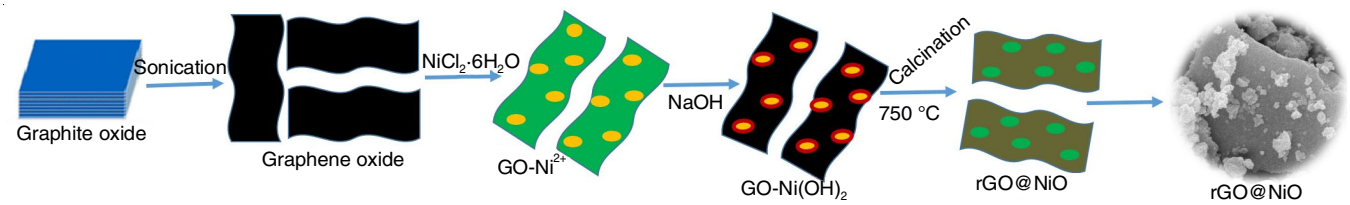

Fig. 3. Schematic representation of the synthesis of rGO@NiO nanocomposites

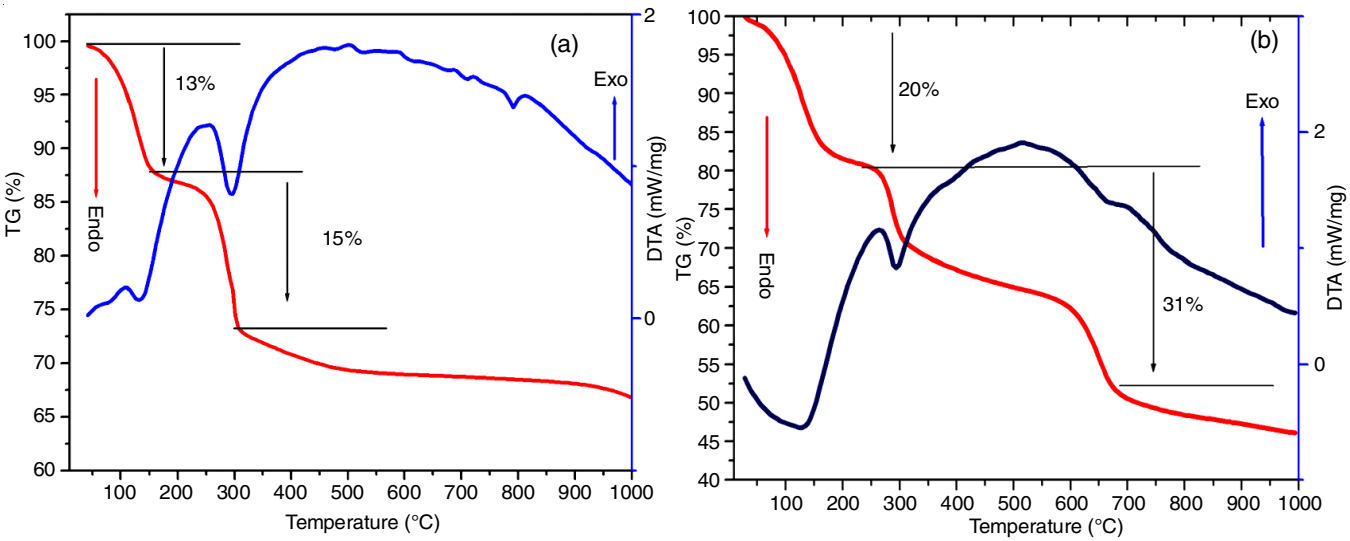

Fig. 4. (a) TG-DTA curve of NiO (b) TG-DTA curve of rGO@NiO

of rGO@NiO. Here the first weight loss occurs at about 287 ºC with 20% weight loss due to dehydration and evaporation of free water from the starting precursor and consecutive weight loss occurs at 694 ºC about 31% weight loss due to dihydroxylation of rGO/Ni(OH)$_2$. Finally, the TGA analysis confirms the required temperature range for the formation of rGO@NiO nanocomposite.

X-ray diffraction analysis: The TG-DTA analysis revealed that NiO and rGO@NiO nanomaterials were formed at around 450 and 750 ºC, respectively from its precursors Ni(OH)$_2$ and rGO/(NiOH)$_2$. XRD patterns of NiO, GO and rGO@NiO nanomaterials in various profile peaks and the diffraction angle 2θ ranges from 10º to 80º are represented in Fig. 5.

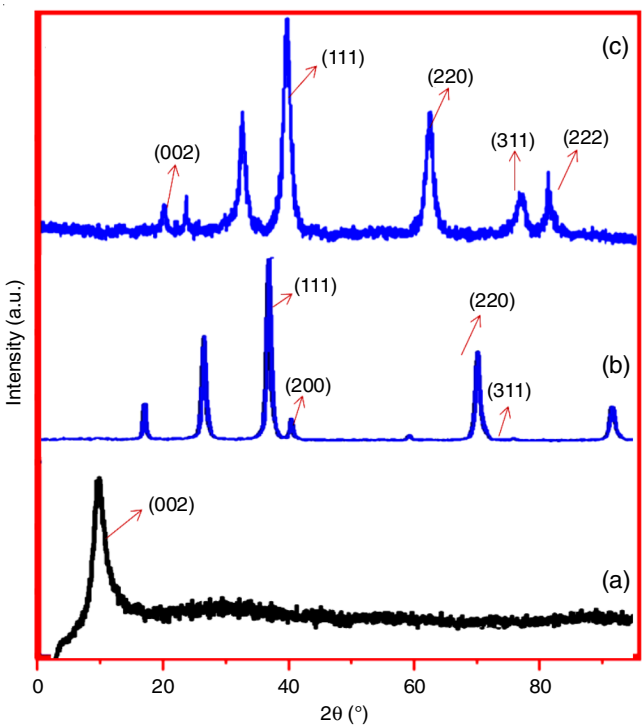

Fig. 5. XRD patterns of the synthesized a) GO, b) NiO and c) rGO@NiO

The XRD patterns of the calcined samples exhibited sharper reflection peaks confirmed the good crystallinity and the fine grain size [25,26]. The observed diffraction peaks and other calcinated values are presented in Table-1. For NiO, the peaks appearing at 2θ = 37.27º, 43.33º, 62.92º and 75.45º can be readily correlated for (111), (200), (220) and (311) crystal planes of the bulk NiO. For GO, the XRD pattern centred at 2θ = 11.4º is indexed for (002) plane of GO. The XRD pattern observed at 2θ = 22.74º, 39.33º, 44.76º, 64.51º and 77.63º can be readily responsible for (002), (111), (200), (220) and (311) crystal planes of the rGO@NiO nanocomposites. By comparing these data with known standard data published by the Joint Committee on Powder Diffraction Standards (JCPDS Card No: 47-1049) [27], it is clear that the NiO and rGO@NiO nanoparticles exhibited in cubic phase crystal nature [28]. The structural parameters were calculated such as crystallite size, microstrain and dislocation density of rGO@NiO from Debye-Scherer's formula [29] given by the eqns. 1-3 and the values are presented in Table-1.

$$\text{Crystalline size (D)} = \frac{0.9\lambda}{\beta\cos\theta} \quad (1)$$

$$\text{Dislocation density } (\delta) = \frac{1}{D2} \quad (2)$$

$$\text{Macrostrain } (\varepsilon) = \frac{\beta\cos\theta}{4} \quad (3)$$

where λ is the wavelength (λ = 1.546 Å) (CuK$_\alpha$), β is the full width at half maximum (FWHM) of the line and θ is the diffraction angle. The lattice parameters and volume have also been calculated using the following eqns. 4 and 5 for the cubic system [30,31] and are given in Table-1.

$$a = d\sqrt{h^2 + k^2 + l^2}\text{Å} \quad (4)$$

and

$$V = a^3(m^3) \quad (5)$$

Williamson-Hall method: The crystallite size (D) and strain (ε) values were also calculated using the Williamson-Hall (W-H) method according to eqn. 6 [32].

$$\frac{\beta\cos\theta}{\lambda} = \frac{1}{D} + \sum\frac{\text{Sin}\theta}{\lambda} \quad (6)$$

where β is the full width at half maximum of the line, λ is the wavelength of the X-ray source used (1.5406 Å) and θ is the Bragg angle. From the plots of β cos θ/λ *versus* sin θ/λ (Fig. 6), the crystallite size and strain values are calculated from the reciprocal of the intercept on the Y-axis and the slope, respectively. The crystallite size and strain values were reproduced

TABLE-1
STRUCTURAL PARAMETERS OF NiO, GO AND rGO@NiO

Sample	d-spacing (Å)	FWHM (β)	Macrostrain $\varepsilon \times 10^{-3}$	Dislocation density $\delta \times 10^{15}$ (m^{-2})	Average crystallite size (nm)	Lattice parameter (Å) & Volume (m^3)
NiO	2.4106	0.434	1.7934	2.6768	18.689	a= 4.716, V= 72.87
	2.0863	0.435	1.7629	2.5867		
	1.4760	0.507	1.8860	2.9604		
	1.2589	0.578	1.9937	3.3080		
GO	1.6748	0.498	4.9648	1.2941	27.798	a= 2.47, V= 35.88
rGO@NiO	2.3102	0.363	4.8667	3.7895	18.126	a= 4.177, V= 72.88
	1.9199	0.363	3.6745	2.5951		
	1.3370	0.372	2.8045	2.2876		
	1.2315	0.432	2.5581	2.1604		
	1.7655	4.799	3.7812	1.2369		

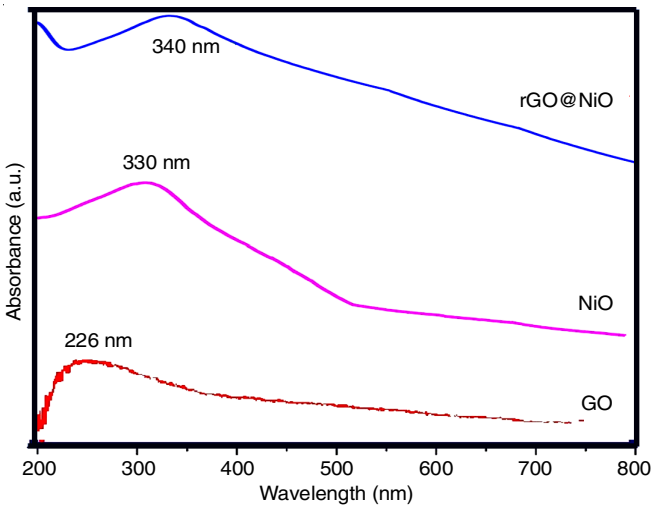

Fig. 6. UV-Visible spectrum of GO, NiO and rGO@NiO nanocomposite

(Table-2) which almost matched with the data reported by Debye-Scherer method. The Debye-Scherer and Williamson-Hall method results are tabulated in Table-3.

TABLE-2
CRYSTALLITE SIZE AND MACROSTRAIN FOR THE NiO AND rGO@NiO NANOCOMPOSITE

Samples	Crystallite size (D) (nm)	Macrostrain (ε) × 10^{-3}
NiO	21.8590	2.9446
rGO@NiO	21.3460	2.6604

TABLE-3
COMPARISON OF DEBYE-SCHERRER AND W-H METHOD

Sample	Method	Crystallite size (D) (nm)	Microstrain (ε) × 10^{-3}
NiO	Debye-Scherrer's	18.6887	1.2797
	W-H Method	21.8590	2.9446
rGO@NiO	Debye-Scherrer's	18.1256	1.3038
	W-H Method	21.3460	2.6604

The UV-vis spectra of NiO, rGO and rGO@NiO nanocomposites are reproduced in Fig. 6. In these studies, NiO nanoparticles show an absorption peak at 317 nm, the GO absorption peak is observed at 226 nm whereas the rGO@NiO display an absorption peak around at 340 nm. The strongest absorption band at 317 nm for the NiO is shifted to a lower absorption band at around 340 nm in the presence of GO, indicating the successful formation of rGO@NiO nanocomposite. The optical bandgap is calculated from the following eqn. 7 and the observed band gap value of GO, NiO and rGO @NiO nano samples are 5.40, 3.75 and 3.64 eV, respectively. The bandgap of rGO@NiO nanocomposite was calculated as 3.64 eV and it has redshift to that of bulk NiO (3.75 eV), which could be ascribed to the interaction of NiO with the graphene backbone and large surface of rGO@NiO nanocomposites which is very useful for photodegratation processes [33].

$$Eg = \frac{hc}{\lambda} \quad (7)$$

where, h = Planck's constant, c = velocity, λ = wavelength.

FT-IR spectral analysis: The FT-IR spectrum of NiO, GO and rGO@NiO nanocomposites are presented in Fig. 7. The sharp peaks at 427 and 416 cm^{-1} can be ascribed to the Ni-O stretching vibrational modes and confirmed the formation of NiO and rGO@NiO spinel structure [34]. The characteristic peaks observed around 1632 and 3447 cm^{-1} are attributed to the O-H stretching mode of water molecules adsorbed on the surface of the nanomaterials [35,36].

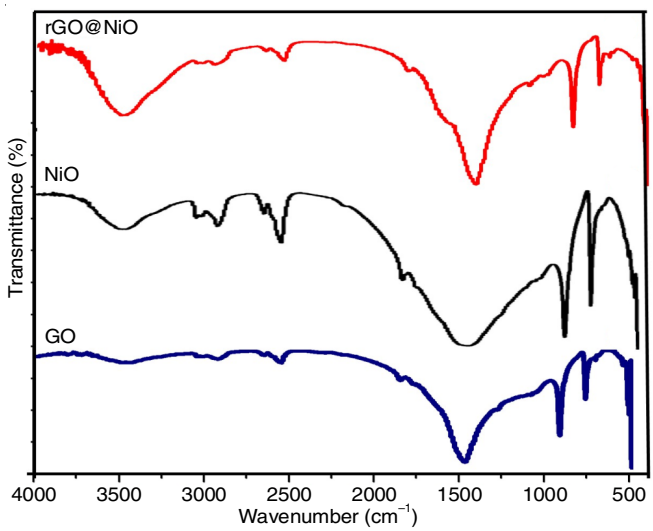

Fig. 7. FT-IR spectrum of NiO, GO and rGO@NiO nanocomposite

Morphology analysis: The morphology of the graphene oxide/nickel oxide nanocomposite was investigated with a scanning electron microscope (SEM, LEO-0430, Cambridge) at room temperature, mounted directly onto sample stub and coated with gold film (~ 200 nm) under reduced pressure (0.133 Pa). The SEM images of pure rGO, NiO and rGO@NiO composite is shown in Fig. 8. Fig. 8a and 8b revealed that the pure NiO looks like non-uniform spherical shape and the entire architecture is built from a smooth surface, of which the thickness is about 10-20 nm. It is evident that (Fig. 8b and 8c) GO is almost transparent and GO layers interact with each other to form a 3D network with voids. The SEM images of the rGO@NiO nanocomposite (Fig. 8e and 8f) are compared with the image of GO and revealed that the surface of rGO@ NiO composite is much rougher than that of GO, which might be attributed to the uniform distribution of NiO nanoparticles on GO [37].

Elemental analysis (EDAX): The EDX spectrum of the NiO and rGO@NiO nanocomposite is presented in Fig. 9. The prominence of the presence of nickel (Ni = 70.21%) and oxygen (O = 29.79%) peaks confirmed the presence of NiO nanoparticles. In rGO@NiO nanocomposite similarly, the presence of nickel (N = 31.87%), carbon (C = 36.60%) and oxygen (O = 31.53%) peaks further reveals the successful formation of the rGO@NiO nanocomposite. No extra peaks were obtained for any of the samples, indicating purity of the synthesized products [28].

TEM analysis: TEM measurement was carried out to get more information about the morphology and crystallinity of the samples. TEM image of GO is reproduced in Fig. 10 and

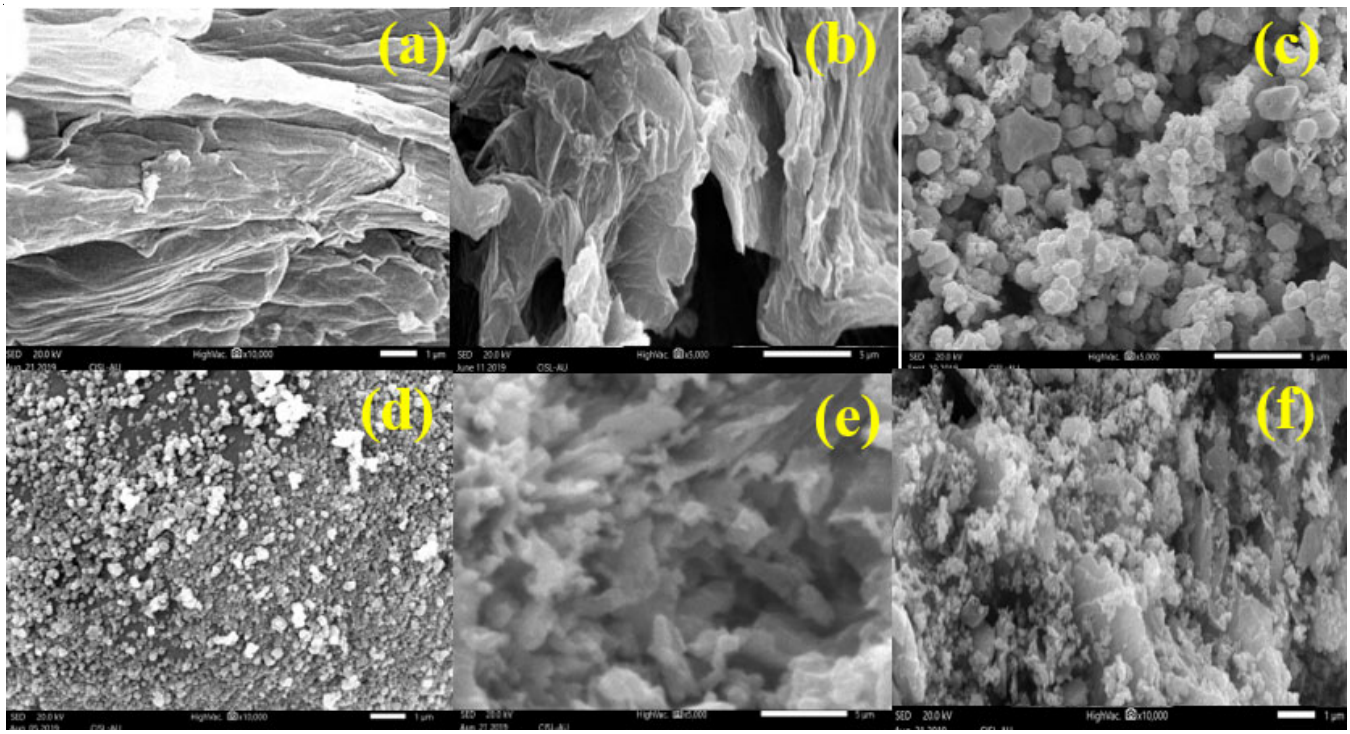

Fig. 8. SEM images of rGO, NiO and rGO@NiO nanocomposite (a) and (b) rGO, (c) and d) NiO, (e) and f) rGO@NiO

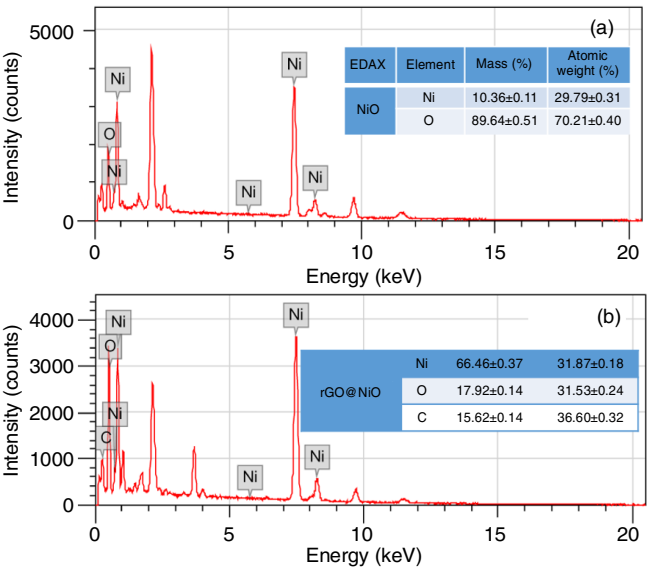

Fig. 9. EDAX spectra of NiO and rGO@NiO nanocomposite

revealed that the rGO is transparent and flexible in nature. Fig. 10b and 10c are the TEM images of NiO and the images informed the presence of spherical and hexagonal shaped NiO crystals. The TEM image of rGO@NiO depicted in Fig. 11d and this image informed that the spherical and hexagonal shaped NiO crystals are decorated on the smooth surface of rGO. The average size of the NiO particles are around 10 nm and it is a good agreement with the particle size deduced from the XRD analysis [38-40].

Cyclic voltammetry (CV) studies: Cyclic voltammetry measurements (CV) were performed in a potential range between -1.2 to 1.4 mV s^{-1} to examine the electrochemical characteristics of the prepared GO, NiO and rGO@NiO electrode. Fig. 11 represents the CV curves of GO, NiO and rGO@NiO nanocomposite with the scan rates of 10, 30, 50 and 100 mV s^{-1}. A pair of well-defined broad redox reaction peaks visible in the CV curves indicating that the electrochemical capacitance of the composite mainly results from the pseudo capacitance [41]. Furthermore, the peak current increases with increasing scan rate from 10 to 100 mV s^{-1}, which suggest its good reversibility of fast charge-discharge response. The specific capacitance of the synthesized GO, NiO and rGO@ NiO nanomaterials can be calculated using eqn. 8:

$$Cs = \frac{\int Idt}{mv} \quad (8)$$

The plot of specific conductance *versus* scan rate (Fig. 11f) indicated that the specific capacitance values are inversely related with scan rates. The specific capacitance of NiO, GO and rGO@NiO nanomaterials are 76, 167 and 233 F g^{-1}, respectively at the scan rate of 10 mV s^{-1}. The CV data implied that rGO@NiO nanocomposite has higher capacitance character than that of pure GO and NiO nanoparticles. As the scan rate increases the average specific capacitance have reduced to 97 F g^{-1} in NiO, 38 F g^{-1} in GO and 37 F g^{-1} in rGO@NiO at the scan rate of 100 mV s^{-1} suggesting that rGO@NiO nanocomposite owns better stability and good conductivity to scan rates [42].

Electrochemical impedance spectroscopy (EIS): The electrochemical impedance spectroscopy (EIS) technique is a powerful tool for characterizing the electrochemical process occurring at the solution/electrode interface. Fig. 12 shows the Nyquist plots of NiO and rGO@NiO electrodes. Partial semi-circle in the high-frequency region and a straight line in

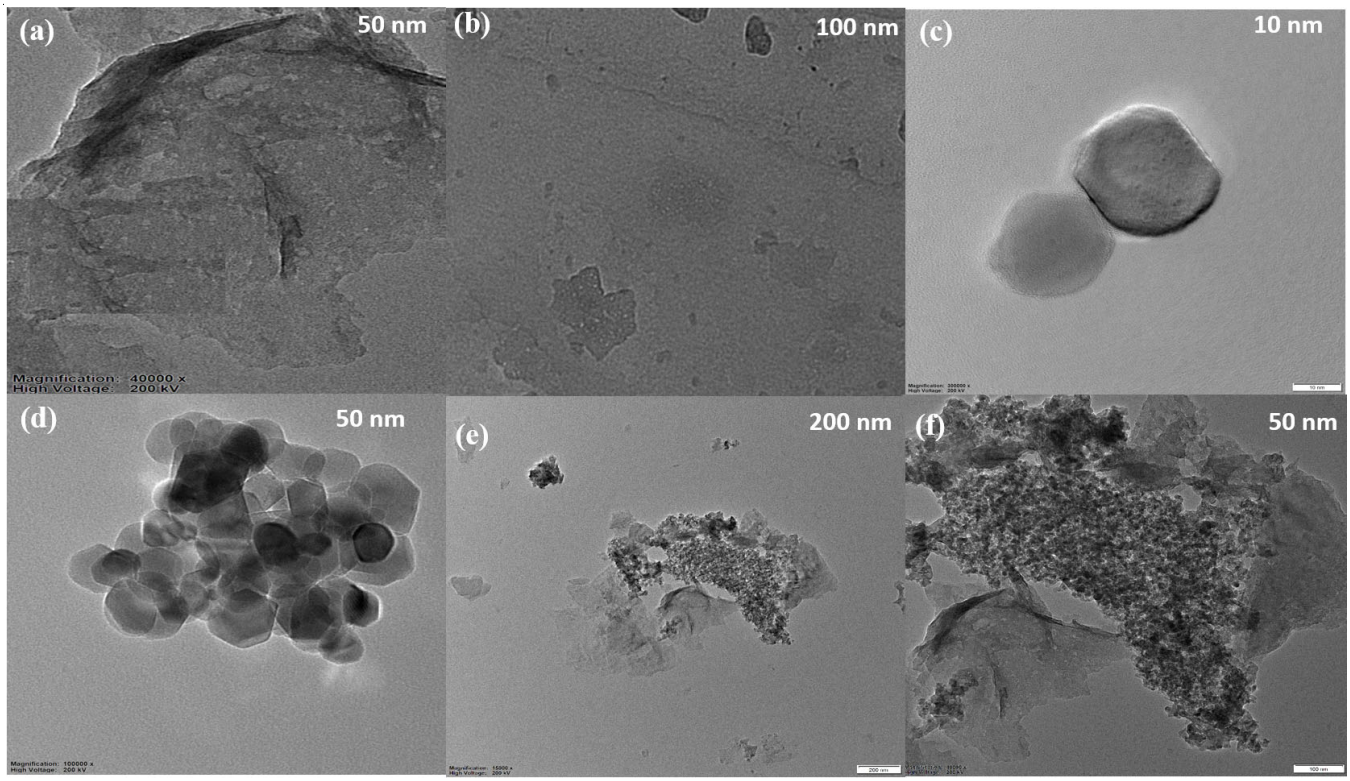

Fig. 10. TEM images of NiO, rGO and rGO@NiO nanocomposite (a) and (b) rGO, (c) and (d) NiO, (e) and (f) rGO@NiO

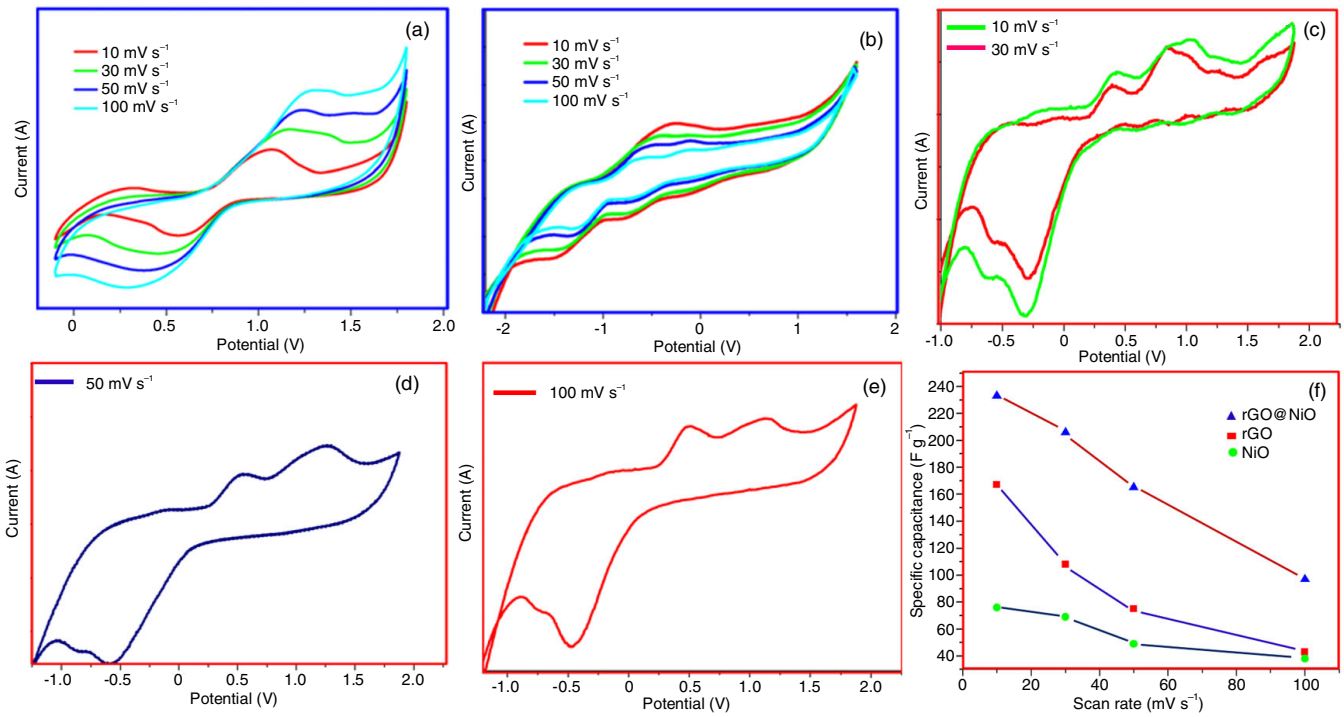

Fig. 11. Cyclic voltgrame of rGO@NiO nanocomposite (a) NiO, (b) rGO, (c) to (e) rGO@NiO nanocomposite and (f) specific capacitance variations at different scan rates of NiO, rGO and rGO@NiO

the low-frequency region (Fig. 12a,b) is seen in the plots. The high-frequency arc is related to the charge transfer resistance (R_{ct}) between the electroactive material and electrolyte interface shows the real and imaginary parts of the impedance as the *x*- and *y*-axes on the Nyquist plot [43]. This line is parallel to the imaginary axis indicating an ideal behaviour. It represents the ion diffusion in the structure of the electrode materials. After adding NiO the conductivity of the electrode is increased and therefore, the radius of the semicircle is decreased with the effect of smaller charge transfer resistance. In the low-frequency

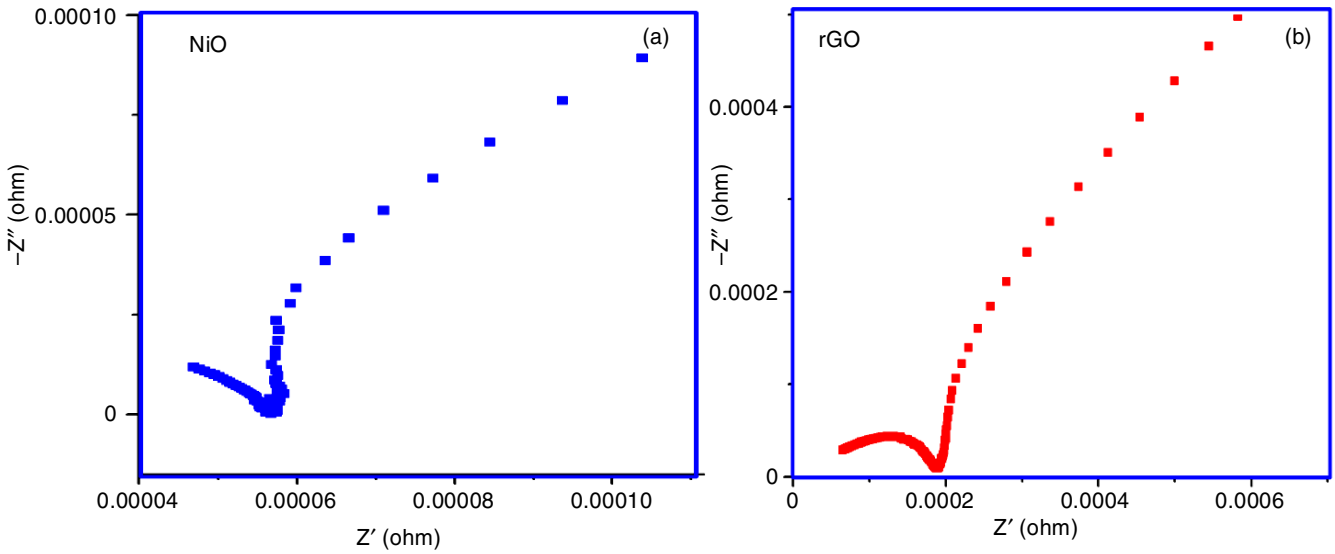

Fig. 12. Nyquist plots of the NiO and rGO@NiO nanocomposite

region, the impedance plot of GO assisted NiO electrode exhibits a nearly straight line a limiting diffusion process, which is a characteristic feature of pure capacitive behaviour. The EIS result confirmed that NiO nanoparticles were well-separated on the GO surface. Therefore, rGO@NiO acted as an excellent electronic substrate with high electron transfer passages [44-46].

Photocatalytic activity and its mechanism: Initially, the UV-vis spectrum was recorded for the different mole concentrations (10^{-2}, 10^{-3}, 10^{-4} and 10^{-5} M) of both methyl violet and rhodamine B dyes. According to the results, the concentrations were optimized as 10^{-4} M for both the dyes to carry out the degradation process. To find the degradation time of dyes, different quantities of rGO@NiO *viz.*, 5, 10, 15, 20, 25 and 30 mg was added as a catalyst into the dye solutions and the systems were kept in sunlight with continuous stirring. The system was observed by the naked eye and fixed the effective degradation time as 60 min for 20 mg of rGO@NiO catalyst in methyl violet and 30 mg of rGO@NiO catalyst in rhodamine B dyes. The UV-vis absorption peaks observed for methyl violet and rhodamine B without the catalyst was 244, 298, 575 nm (major peak) and 259, 356, 554 nm (major peak), respectively. When the catalyst was added into the dye solutions the absorption peaks of dyes were started to vanish and the samples (5 mL) were collected in every 10 min for the UV analysis. The peaks observed at 575 for methyl violet and 554 nm for rhodamine B have vanished nearer to 60 min with approximately 92% of degradation. The percentage of photocatalytic degradation was calculated using eqn. 9:

$$\text{Photodegradation efficiency } (\%) = \frac{C_o - C_t}{C_o} \times 100 \quad (9)$$

Photodegradation reaction of dyes can be described using Langmuir-Hinshelwood kinetic model [47] and the photocatalytic activity of the catalyst can be evaluated using eqn. 10:

$$\ln\left(\frac{C_o}{C_t}\right) = kt \quad (10)$$

where C_o and C_t are the initial concentration of dye solutions and at irradiation time 't', respectively and k is the pseudo-first-order rate constant. The absorption of methyl violet and rhodamine B dyes with various time profiles are shown in Figs. 13 and 14 and the degradation efficiency is depicted in Fig. 15.

Kinetic studies of photocatalytic degradation using NiO and rGO@NiO: The linear relationship of ln (C_o/C) *vs.* time (Fig. 16) indicated that the photocatalytic degradation of methyl violet and rhodamine B dyes with NiO and rGO@NiO nanocomposite were followed to the pseudo-first-order kinetics [48]. The calculated rate constant of NiO and rGO@NiO photocatalysts were 0.03929 and 0.04429 min^{-1}, respectively for methyl violet whereas the rate constants observed as 0.03286 min^{-1} and 0.04679 min^{-1}, respectively for the rhodamine B dyes. The observed rate constant values revealed that the photocatalytic activity of rGO@NiO catalyst is approximately 13% for methyl violet-dye and 42 % for rhodamine B dye have been more efficient than the NiO photocatalyst.

Mechanism of photocatalytic activity: Photogeneration of electron-hole pair between conduction and valence bands is generally responsible for the degradation of dye pollutant in photocatalytic decomposition processes. Photogenerated h^+ in the valence band reacts with H_2O to produce the $OH^\bullet$ and this very reactive $OH^\bullet$ is completely responsible for the dye degradation process [49]. The schematic representation of photocatalytic degradation of NiO and rGO@NiO photocatalyst under sunlight is shown in Fig. 17. Two different mechanisms are proposed for photocatalytic activities of NiO and rGO@NiO as follows:

$$NiO + h\nu \rightarrow NiO\ (e^-_{cb} + h^+_{vb}) \rightarrow GO\ (e^- + h^+) \quad (11)$$

$$NiO\ (e^-_{cb}) + O_2 \rightarrow O_2^{\bullet-} \quad (12)$$

$$NiO\ (h^+_{vb})\ e^-_{cb} + OH^\bullet \rightarrow OH^\bullet + NiO \quad (13)$$

$$GO\ (e^-) + O_2 \rightarrow O_2^{\bullet-} + GO + H_2O \rightarrow OH^\bullet + GO \quad (14)$$

$$OH^\bullet + Dye \rightarrow CO_2 + H_2O + Intermediates \quad (15)$$

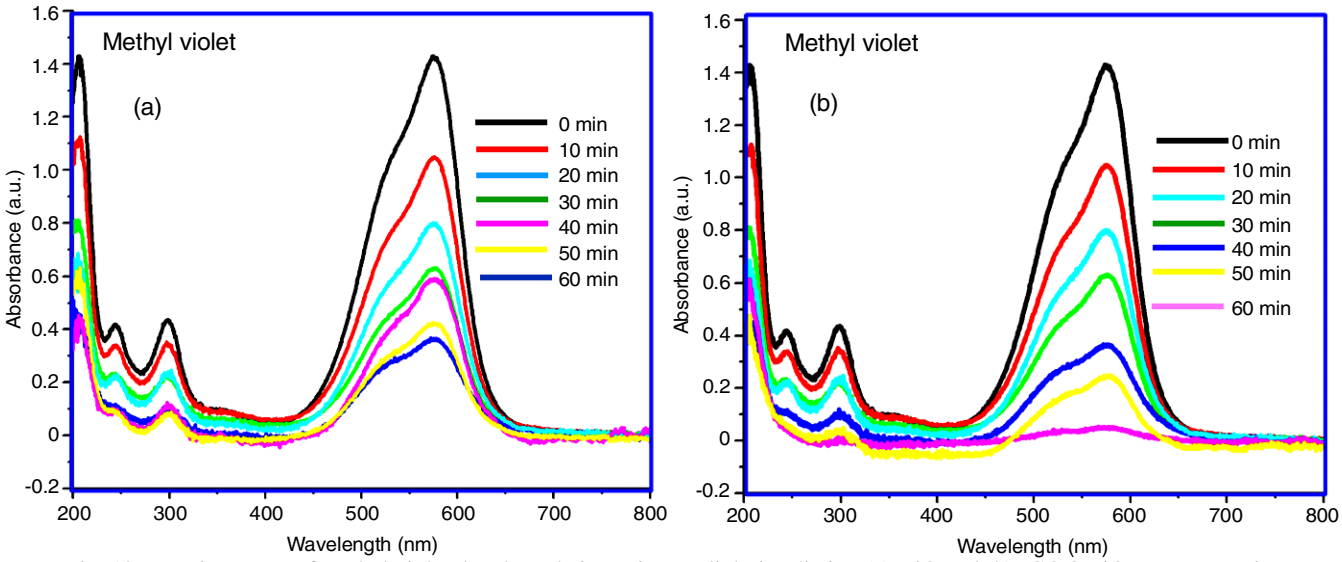

Fig. 13. UV-vis spectra of methyl violet dye degradation using sunlight irradiation (a) NiO and (b) rGO@NiO nanocomposite

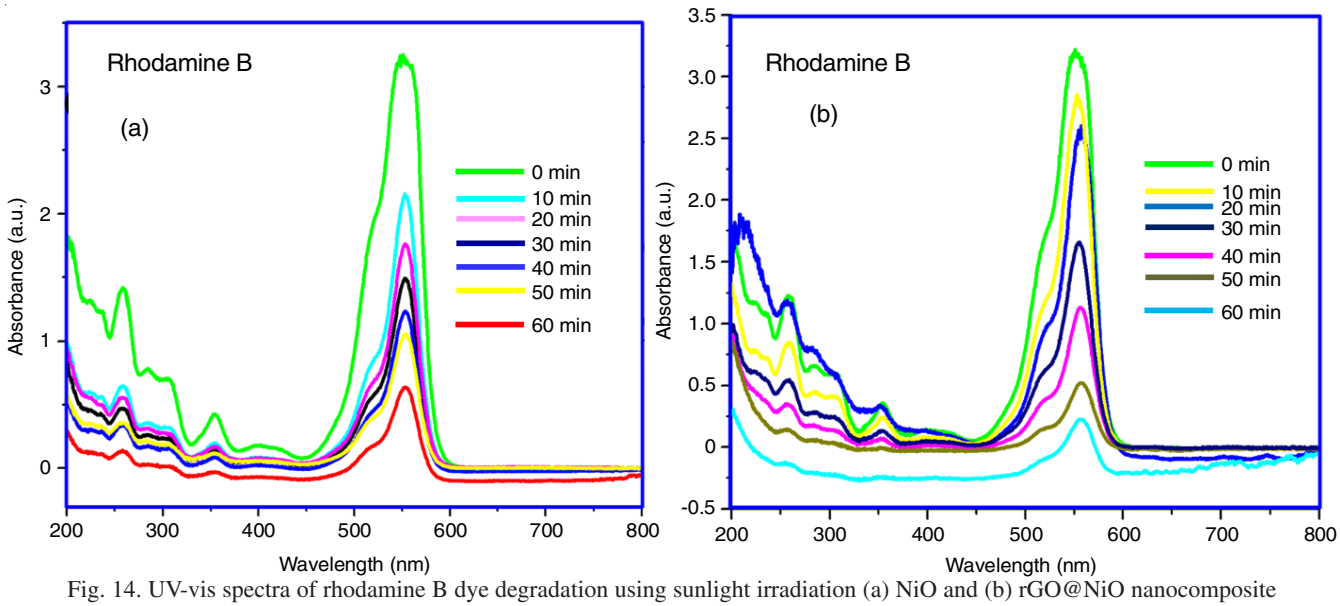

Fig. 14. UV-vis spectra of rhodamine B dye degradation using sunlight irradiation (a) NiO and (b) rGO@NiO nanocomposite

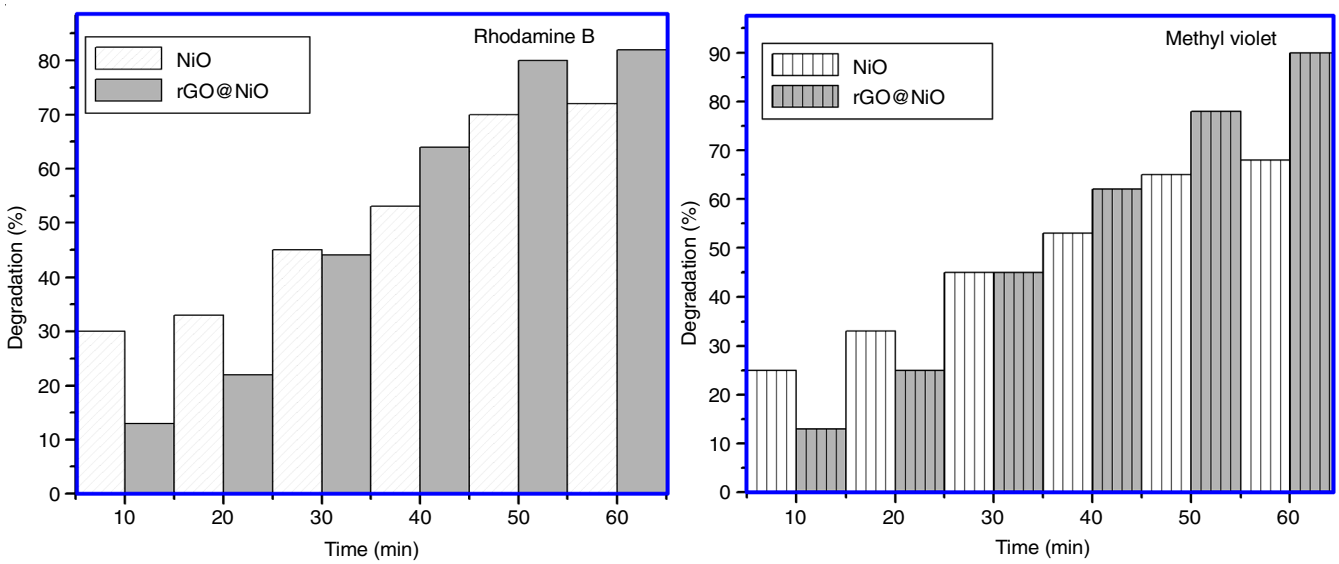

Fig. 15. Degradation % of methyl violet (MV) and rhodamine B (Rh-B)

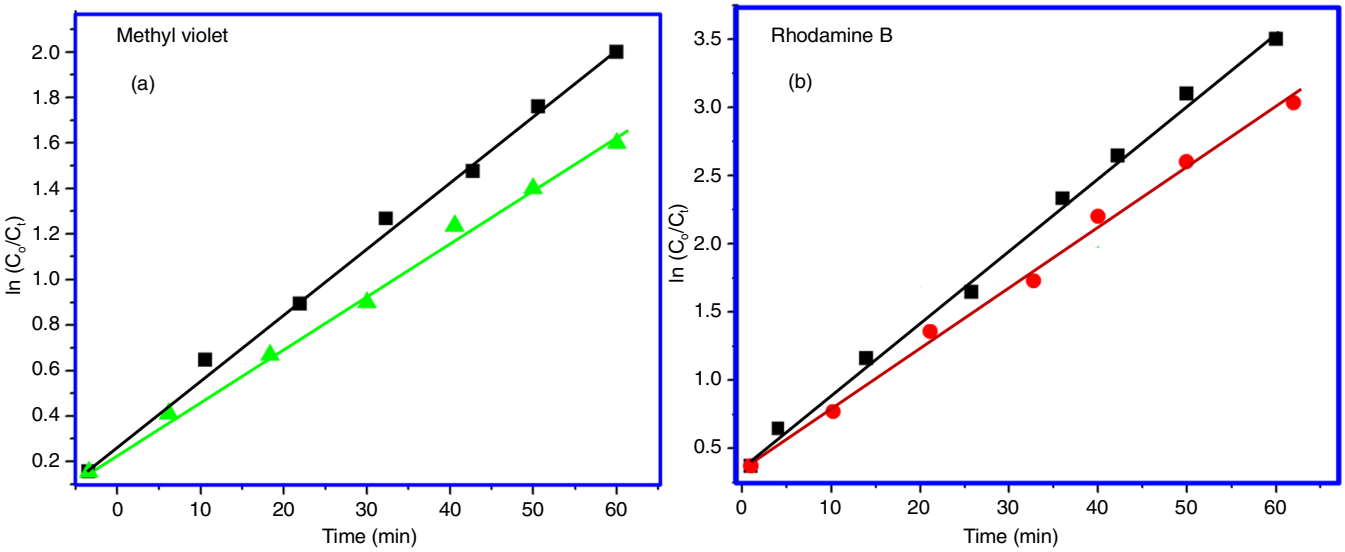

Fig. 16. Pseudo-first order plot for NiO and rGO@NiO

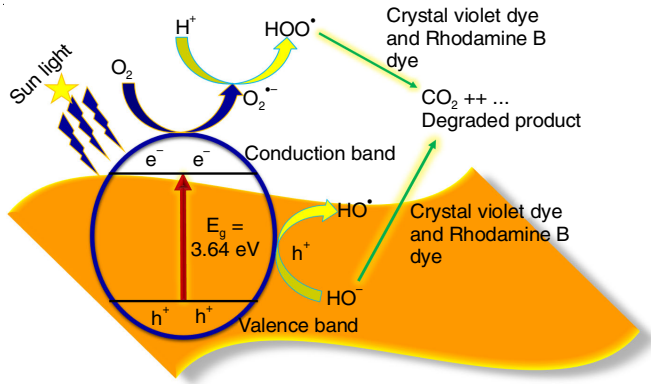

Fig. 17. Schematic representation of photocatalytic degradation of NiO and rGO@NiO photocatalyst under sunlight

Recycle process: To test the stability, the photocatalysts were reused for three times and the results are shown in Fig. 18. The results revealed that the catalysts were maintained the effective photocatalytic activity after the third cycle with the negligible activity loss. Fig. 18b shows the XRD patterns of NiO and rGO@NiO after the third recycling process. The XRD peaks are similar to the fresh samples further confirming the high stability of NiO and rGO@NiO during the degradation process. According to this mechanism, it can be said that graphene layer can postpone the recombination process, so the performance of rGO@NiO nanocomposite is better than pure NiO nanoparticles [50].

Conclusion

In summary, the rGO@NiO nanocomposite as sunlight driven photocatalyst was synthesized by co-precipitation method using NaOH as a mineralizer. Thermal analysis reveals the pure phase formation mechanism of $Ni(OH)_2$ and GO/$Ni(OH)_2$ nanoparticles. The XRD studies proved that NiO was successfully incorporated in the GO sheet to yield the rGO@NiO nanocomposite matrix. The UV-visible spectroscopy showed that the rGO@NiO composites have stronger absorption than pure GO and NiO nanoparticles. The EDS spectrum confirmed the purity of the rGO@NiO nanocomposites and the TEM image confirmed the spherical morphology of NiO crystallites occupied on the surface of the GO layer. The CV and EIS results revealed that the rGO@NiO nanocomposite has lower resistance and good conducting nature than the pure GO and NiO. The synthesized rGO@NiO nanocomposites exhibited

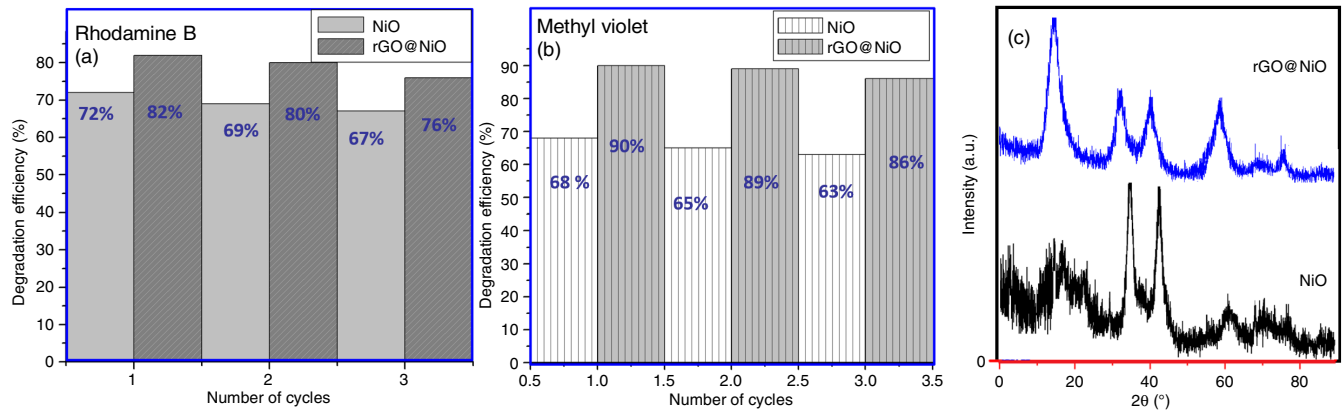

Fig. 18. (a and b) Stability of NiO and rGO@NiO photocatalyst using methyl violet and rhodamine B dye, (c) XRD pattern of dye recycled nanocomposite after three cycles

improved photocatalytic performance than the pure GO and NiO nanoparticles. Significantly, by virtue of these characteristics, the rGO@NiO nanocomposites is a promising material for the development of high-performance supercapacitors and the remediation of polluted water.

CONFLICT OF INTEREST

The authors declare that there is no conflict of interests regarding the publication of this article.

REFERENCES

1. M.-H. Li, J.-H. Yum, S.-J. Moon and P. Chen, *Energies*, **9**, 331 (2016); https://doi.org/10.3390/en9050331
2. B. Tong and M. Ichimura, *Electr. Commun. Jpn*., **101**, 45 (2018); https://doi.org/10.1002/ecj.12043
3. S. Azizighannad and S. Mitra, *Sci. Rep.*, **8**, 10083 (2018); https://doi.org/10.1038/s41598-018-28353-6
4. T. Tubthong, A. Wisitsoraat, C. Tansarawiput, P. Opaprakasit and P. Sreearunothai, Development of Ammonia Gas Sensor Based on Ni-Doped Reduce Graphene Oxide, Proceedings of the 4th International Conference on Engineering, Applied Sciences and Technology (ICEAST 2018), 4-7 July 2018, Phuket, Thailand, pp. 760-763 (2018).
5. S.Sadhukhan, A. Bhattacharyya, D. Rana, T.K. Ghosh, J.T. Orasugh, S. Khatua, K. Acharya and D. Chattopadhyaya, *Mater. Chem. Phys.*, **247**, 122906 (2020); https://doi.org/10.1016/j.matchemphys.2020.122906
6. H. Ren, C. Gu, S.W. Joo, J. Zhao, Y. Sun and J. Huang, *Sens. Actuators B*, **266**, 506 (2018); https://doi.org/10.1016/j.snb.2018.03.130
7. M. Zannotti, E. Benazzi, L.A. Stevens, M. Minicucci, L. Bruce, C.E. Snape, E.A. Gibson and R. Giovannetti, *ACS Appl. Energy Mater*., **2**, 7345 (2019); https://doi.org/10.1021/acsaem.9b01323
8. S.P. Deshmukh, D.P. Kale, S. Kar, S.R. Shirsath, B.A. Bhanvase, V.K. Saharan and S.H. Sonawane, *Nano-Struct. Nano-Objects*, **21**, 100407 (2020); https://doi.org/10.1016/j.nanoso.2019.100407
9. X. Li, Y. Zhao, X. Wang, J. Wang, A.M. Gaskov and S.A. Akbar, *Sens. Actuators B*, **230**, 330 (2016); https://doi.org/10.1016/j.snb.2016.02.069
10. G.S. Han, Y.H. Song, Y.U. Jin, J.-W. Lee, N.-G. Park, B.K. Kang, J.-K. Lee, I.S. Cho, D.H. Yoon and H.S. Jung, *ACS Appl. Mater. Interfaces*, **7**, 23521 (2015); https://doi.org/10.1021/acsami.5b06171
11. S. Xu, F. Sun, S. Yang, Z. Pan, J. Long and F. Gu, *Sci. Rep*., **5**, 8939 (2015); https://doi.org/10.1038/srep08939
12. S. Yao, S. Zhou, J. Wang, W. Li and Z. Li, *Photochem. Photobiol. Sci*., **18**, 2989 (2019); https://doi.org/10.1039/C9PP00242A
13. R. Liu, R. Qiu, T. Zou, C. Liu, J. Chen, Q. Dai, S. Zhang and H. Zhou, *Nanotechnology*, **30**, 075202 (2018); https://doi.org/10.1088/1361-6528/aaf2ad
14. S. Kumar, R.D. Kaushik, G.K. Upadhyay and L.P. Purohit, J. Hazard. Mater., 124300 (2020); https://doi.org/10.1016/j.jhazmat.2020.124300
15. V. Galstyan, E. Comini, I. Kholmanov, G. Faglia and G. Sberveglieri, *RSC Adv*., **6**, 34225 (2016); https://doi.org/10.1039/C6RA01913G
16. Z. Zhan, L. Zheng, Y. Pan, G. Sun and L. Li, *J. Mater. Chem.*, **22**, 2589 (2012); https://doi.org/10.1039/C1JM13920G
17. T. Lv, Z. Xu, W. Hong, G. Li, Y. Li and L. Jia, *Chem. Eng. J*., **382**, 123021 (2020); https://doi.org/10.1016/j.cej.2019.123021
18. N. Karikalan, M. Velmurugan, S.-M. Chen and C. Karuppiah, *ACS Appl. Mater. Interfaces*, **8**, 22545 (2016); https://doi.org/10.1021/acsami.6b07260
19. C. Zhang, Q. Chen and H. Zhan, *ACS Appl. Mater. Interfaces*, **8**, 22977 (2016); https://doi.org/10.1021/acsami.6b05255
20. P.E. Lokhande and U.S. Chavan, *Mater. Sci. Energy Technol.*, **2**, 52 (2019); https://doi.org/10.1016/j.mset.2018.10.003
21. Y. Zou and Y. Wang, *Nanoscale*, **3**, 2615 (2011); https://doi.org/10.1039/C1NR10070J
22. S. Wu, R. Xu, M. Lu, R. Ge, J. Iocozzia, C. Han, B. Jiang and Z. Lin, *Adv. Energy Mater*., **5**, 1500400 (2015); https://doi.org/10.1002/aenm.201500400
23. F. Gao, Q. Wei, J. Yang, H. Bi and M. Wang, *Ionics*, **19**, 1883 (2013); https://doi.org/10.1007/s11581-013-0939-5
24. F. Basharat, U.A. Rana, M. Shahid and M. Serwar, *RSC Adv.*, **5**, 86713 (2015); https://doi.org/10.1039/C5RA17041A
25. S. Min, C. Zhao, Z. Zhang, G. Chen, X. Qian and Z. Guo, *J. Mater. Chem. A*, **3**, 3641 (2015); https://doi.org/10.1039/C4TA06233G
26. N. Parveen, S.A. Ansari, S.G. Ansari, H. Fouad and M.H. Cho, *New J. Chem*., **41**, 10467 (2017); https://doi.org/10.1039/C7NJ01915G
27. W. Ni, B. Wang, J. Cheng, X. Li, Q. Guan, G. Gu and L. Huang, *Nanoscale*, **6**, 2618 (2014); https://doi.org/10.1039/C3NR06031D
28. A.Al-Nafieya, A. Kumar, M. Kumar, A. Addad, B. Sieber, S. Szunerits, R. Boukherroub and S.L. Jain, *J. Photochem. Photobiol. A*, **336**, 198 (2017); https://doi.org/10.1016/j.jphotochem.2016.12.023
29. D.L. Fang, Z.D. Chen, X. Liu, Z.F. Wu and C.H. Zheng, *Electrochim. Acta*, **81**, 321 (2012); https://doi.org/10.1016/j.electacta.2012.07.047
30. A. Shanmugasundaram, N.D. Chinh, Y.-J. Jeong, T.F. Hou, D.-S. Kim, D. Kim, Y.-B. Kim and D.-W. Lee, *J. Mater. Chem. A*, 7, 9263 (2019); https://doi.org/10.1039/C9TA00755E
31. C.A. Zito, T.M. Perfecto, C.S. Fonseca and D.P. Volanti, *New J. Chem*., **42**, 8638 (2018); https://doi.org/10.1039/C8NJ01061G
32. R.M. Chellab and K.H. Harbbi, *AIP Conf. Proc.*, **2123**, 020044 (2019); https://doi.org/10.1063/1.5116971
33. P. Ahuja, S.K. Ujjain, I. Arora and M. Samim, *ACS Omega*, **3**, 7846 (2018); https://doi.org/10.1021/acsomega.8b00765
34. N.D.M. Ridzuan, M.S. Shaharun, K.M. Lee, I.U. Din and P. Puspitasari, Catalysts, **10**, 471 (2020); https://doi.org/10.3390/catal10050471
35. A. Roychoudhury, A. Prateek, S. Basu and S.K. Jha, *J. Nanopart. Res*., **20**, 70 (2018); https://doi.org/10.1007/s11051-018-4173-y
36. F.A.A. Al-Rub, M.M. Fares and A.R. Mohammad, *RSC Adv.*, **10**, 37050 (2020) https://doi.org/10.1039/D0RA05530A
37. Z. Jurasz, K. Adamaszek, R. Janik, Z. Grzesik and S. Mrowec, *Defect and Diffusion Forum*, **289-292**, 775 (2009) https://doi.org/10.4028/www.scientific.net/DDF.289-292.775
38. L.A. García-Cerda, K.M. Bernal-Ramos, S.M. Montemayor, M.A. Quevedo-López, R. Betancourt-Galindo and D. Bueno-Báques, *J. Nanomater*., **2011**, 162495 (2011); https://doi.org/10.1155/2011/162495
39. S.P. Jahromi, A. Pandikumar, B.T. Goh, Y.S. Lim, W.J. Basirun, H.N. Lim and N.M. Huang, *RSC Adv*., **5**, 14010 (2015); https://doi.org/10.1039/C4RA16776G
40. A.A. Barzinjy, S.M. Hamad, S. Aydin, M.H. Ahmed and F.H.S. Hussain, *J. Mater. Sci.: Mater. Electron*., **31**, 11303 (2020); https://doi.org/10.1007/s10854-020-03679-y
41. G. Vinodhkumar, J. Wilson, S. Mahalakshmi, V. Ragavendran and A.C. Peter, *Mater. Today Proc.*, (2019); https://doi.org/10.1016/j.matpr.2019.06.004
42. P. Khandagale and D. Shinde, *Int. J. Adv. Res.*, **5**, 1333 (2017); https://doi.org/10.21474/IJAR01/4253

43. E. Nouri, M.R. Mohammadi and P. Lianos, *ACS Omega*, **3**, 46 (2018); https://doi.org/10.1021/acsomega.7b01775
44. J. Gui, J. Zhang, T. Liu, Y. Peng and J. Chang, *New J. Chem*., **41**, 10695 (2017); https://doi.org/10.1039/C7NJ02267K
45. H. Zhang, X. Tian, C. Wang, H. Luo, J. Hu, Y. Shen and A. Xie, Appl. Surf. Sci., **314**, 228 (2014); https://doi.org/10.1016/j.apsusc.2014.06.172
46. Y. Liu, C. Gao, Q. Li and H. Pang, *Chem. Eur. J*., **25**, 2141 (2019); https://doi.org/10.1002/chem.201803982
47. F. Motahari, M.R. Mozdianfard, F. Soofivand and M. Salavati-Niasari, *RSC Adv*., **4**, 27654 (2014); https://doi.org/10.1039/C4RA02697G
48. R. Dewangan, A. Hashmi, A. Asthana, A.K. Singh and M.A.B. Hasan Susan (2020); https://doi.org/10.1080/03067319.2020.1802443
49. N.M. Julkapli, S. Bagheri and S.B.A. Hamid, *The Scient. World J*., **2014**, 692307 (2014); https://doi.org/10.1155/2014/692307
50. Z. Yan, X. Yu, A. Han, P. Xu and P. Du, J. *Phys. Chem. C*, **118**, 22896 (2014); https://doi.org/10.1021/jp5065402